

Evolution of Phase Strains During Tensile Loading of Bovine Cortical Bone**

By Anjali Singhal,* Fang Yuan, Stuart R. Stock, Jonathan D. Almer, L. Catherine Brinson and David C. Dunand

Synchrotron X-ray scattering is used to measure average strains in the two main nanoscale phases of cortical bone – hydroxyapatite (HAP) platelets and collagen fibrils – under tensile loading at body temperature (37 °C) and under completely hydrated conditions. Dog-bone shaped specimens from bovine femoral cortical bone were prepared from three anatomical quadrants: antero-medial, antero-lateral, and postero-lateral. The apparent HAP and fibrillar elastic moduli – ratios of tensile stress as applied externally and phase strains as measured by diffraction – exhibit significant correlations with the (i) femur quadrant from which the samples are obtained, (ii) properties obtained at the micro-scale using micro-computed tomography, i.e., microstructure, porosity and attenuation coefficient, and (iii) properties at the macro-scale using thermo-gravimetry and tensile testing, i.e., volume fraction and Young's modulus. Comparison of these tensile apparent moduli with compressive apparent moduli (previously published for samples from the same animal and tested under the same temperature and irradiation conditions) indicates that collagen deforms plastically to a greater extent in tension. Greater strains in the collagen fibril and concomitant greater load transfer to the HAP result in apparent moduli that are significantly lower in tension than in compression for both phases. However, tensile and compressive Young's moduli measured macroscopically are not significantly different during uniaxial testing.

[*] Dr. A. Singhal, Dr. F. Yuan, Dr. L. C. Brinson, Dr. D. C. Dunand
Department of Materials Science and Engineering, Northwestern University, Evanston, IL 60208, USA

E-mail: anjalisinghal2007@u.northwestern.edu

Dr. S. R. Stock

Department of Molecular Pharmacology and Biological Chemistry, Feinberg School of Medicine, Northwestern University, Chicago, IL 60611, USA

Dr. J. D. Almer

X-ray Sciences Division, Argonne National Laboratory, Argonne, IL 60438, USA

Dr. L. C. Brinson

Department of Mechanical Engineering, Northwestern University, Evanston, IL 60208, USA

[**] The authors thank Dr. Alix Deymier-Black (NU) for numerous useful discussions throughout this work as well as assistance with the diffraction experiments at the APS beamline 1-ID-C. They also acknowledge Dr. Xianghui Xiao (APS) for his help with the micro-CT experiments at APS beamline 2BM. Use of the Advanced Photon Source was supported by the U.S. Department of Energy, Office of Science, Office of Basic Energy Sciences, under Contract No. DE-AC02-06CH11357.

Bone is a hierarchical structural composite consisting of a complex combination of calcium hydroxyapatite [$\text{Ca}_3(\text{PO}_4)_2(\text{OH})_2$, HAP], collagen and water, whose^[1,2] Mammalian long bones are occasionally subjected to near uniaxial tension, e.g., in primates displaying suspensory behavior and, in particular, brachiation,^[3] and in humans during surgical procedures such as limb lengthening by the Ilizarov technique.^[4] The primary loading modes of long bones are bending or compression;^[5] for bending, depending on the position of the neutral stress axis in the transverse-section of the cortical bone and the curvature of the long bone, regions can experience either a gradient of compressive strains or a combination of tensile and compressive strains.^[6] Therefore, it is important to determine the properties of cortical bone in both tension and compression, which in turn can provide information about deformation in bending mode. Bone forms and remodels in response to the loads experienced in vivo,^[1,7] making its properties heterogeneous and dependent on the location. Thus, it is also important to perform measurements on a population of samples in order to obtain statistically significant and reproducible properties. Also, a more complete understanding of the distribution of stresses

(dependent on the local stiffness which may be different in tension and compression) in the femur will lead to improvements in the design of novel implant materials.^[8]

The strength of cortical bone is greater in compression than in tension due to the different forms of microstructural damage; compressive deformation involves shear-type cracks at planes oblique to the direction of loading, while tensile deformation involves cracks separating various microstructural features, like osteons and lamellae, at their boundaries.^[9,10–12] Three-point bending tests on human cortical bones have shown that, as the specimen is loaded, the inelastic tensile strains become progressively higher than the compressive strains.^[10] Thus, it is clear that tensile failure is the determining mode during failure in bending. Like many anisotropic composite materials,^[13] bone may also exhibit differences between the elastic properties in the tensile and compressive modes. Barak *et al.*^[14] has shown using tests in three-point bending on equine bones that the compressive elastic modulus is significantly ($p < 0.05$) lower than the tensile modulus by 6%. On the other hand, Reilly and Burstein^[11] found no difference between the elastic moduli in human and bovine compact bone during uniaxial tensile and compressive tests of 20 specimens. Riggs *et al.* testing equine radii (26 specimens)^[15] and Dempster and Liddicoat testing human femora, tibiae, and humeri (21 specimens)^[16] did not find differences in the tensile and compressive moduli. One challenge associated with these findings is that the species to species variations in properties^[12,17] further confounds the true variation between tensile and compressive stiffness of bone. Young's modulus of bone depends on a number of other factors such as fraction of secondary Haversian bone,^[18] mineral content,^[19,20] density or porosity,^[19,21] and orientation of collagen fibers.^[22] Yet another factor of considerable importance is the testing environment since the hydration state and temperature significantly affect the properties under investigation.^[23] None of the above studies used body temperature during mechanical tests and only one study (Barak *et al.*^[14]) used completely hydrated conditions. Evans^[24] showed that drying increases the tensile modulus of human cortical bone, and Bonfield and Li^[25] showed that bone's elastic modulus decreases with increasing testing temperature. It is thus important to determine the tensile properties of bone, as close as possible, to physiological conditions.

High-energy X-ray scattering is a technique which has been in use to measure, in situ, the micromechanics of deformation within the phases of metal matrix composites^[26] and is now being increasingly used to assess, in situ, the mechanical response of mineralized biological materials such as bone,^[27–34] antler,^[35] and tooth^[36,37] during mechanical loading. The technique offers a unique capability of measuring strains within the nanoscopic phases of the materials while averaging over the entire thickness of the sample, which can range from a few millimeters to few centimeters. To date, the bulk of the research has focused on compressive deformation and only a few studies have investigated tensile deformation.^[27,31,33]

Since biological samples show high spatial variability in structure (and thus properties), it is important to understand the extent of variability in the measured properties due to the heterogeneity in the samples and to determine the repeatability of the measurement technique. These points are addressed in the present work by combining techniques spanning multiple length scales. Tensile loading tests are performed at body temperature (37 °C), in completely hydrated conditions, on 25 samples taken from different locations in the bovine femur cross-section. The strains in the HAP phase and the fibrils, averaged over a $3.6 \times 10^6 \mu\text{m}^3$ volume, are measured by a combination of wide-angle (WAXS) and small-angle X-ray scattering (SAXS). Macroscopic Young's moduli of complete samples are obtained through conventional tensile testing on millimeter-sized dog-bone samples. The microstructure and porosity of the samples are determined through micro-Computed Tomography (micro-CT). Finally, the phase volume fractions are determined through thermogravimetry. Finite-element modeling is used to simulate the experimental conditions and sample geometry to support the experimental results. These results are compared with existing results from compressive testing by Singhal *et al.*,^[34] which were obtained using the same technique and experimental setup on samples taken from the same animal, in order to understand the differences between the two types of loading with respect to the structure of bone.

1. Materials and Methods

1.1. Sample Preparation

Bovine femurs of an 18-month old Black Angus cow were obtained from a local slaughterhouse (Aurora Packing Company Inc., Aurora, IL, USA) within an hour of slaughter. The bones were cleaned of marrow and attached ligaments using scalpels. Twenty five flat rectangular strips of cortical bone with approximate dimensions $30 \times 10 \times 1.5 \text{ mm}^3$ were cut from three anatomical quadrants in a single cross-section of the femur, close to the mid-diaphyseal region and with the 30 mm dimension parallel to the long direction of the femur. The strips were then mounted on a custom-built vertical and horizontal translational stage, and a high-speed, low-torque abrasion aluminum oxide tip (Dremel rotary tool, Multipro 395) was used to grind the smallest faces into a dog-bone shape (Figure 1). The samples have a central gage length of 5 mm, where the cross-section is constant, and taper slightly over 2.5 mm before reaching a 5 mm shoulder region with greater curvature and a 5 mm grip section. The samples were hydrated with de-ionized water throughout the preparation process. The dimensions of each sample were measured using an optical microscope.

1.2. Scattering Measurements

All the samples were loaded in tension on an MTS-858 hydraulic loading frame, with clamping grips custom-made for tensile testing of small samples. A hydration container made of stiff polymer was attached to the grips, which circulated body temperature (37 °C) phosphate buffered saline

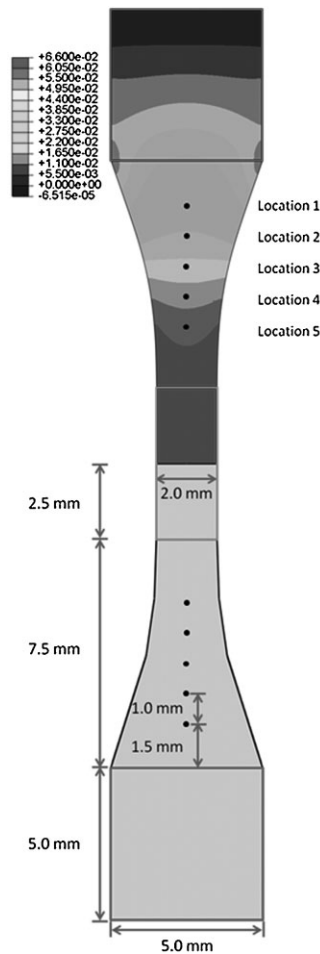


Fig. 1. Sample geometry (to scale). The lower half of the sample shows the scattering (black filled circles) and micro-CT (green box) measurement locations on the tensile sample. The top half of the sample shows a map of longitudinal stresses (expressed in GPa) for a gripping compressive stress of 30 MPa over the gripping section shown by the red box, and an applied tensile load of 183 N (corresponding to 61 MPa in the gage section). The blue box corresponds to the gage section. Scattering measurements are carried out on the lower half of the sample. The measurement locations are overlaid on the stress distribution map in the top half for illustration purpose, given that the sample is symmetrical.

(PBS) around the samples throughout testing. The samples were loaded in steps of 21 N up to a maximal load of 180 N, and unloaded to 0 N in a single step. For each increment of load, WAXS and SAXS patterns (see below) were recorded at five different locations. Due to limited vertical translation range, the lowermost measurement on the sample (Location 1) was in the shoulder region, about 1.5 mm from the top of the lower grip (red box in Figure 1). Measurements were done at a spacing of 1 mm in the vertical direction, as indicated in the bottom half of the sample in Figure 1: Location 5 was thus in the region with a slight taper. The locations marked on the top half of the sample are for illustration purpose, given that the sample is symmetrical. The sample was horizontally centered with respect to the X-ray beam using absorption measurements.

Scattering measurements were performed at station 1-ID-C at APS at two different length scales: WAXS (\AA -level

periodicities) and SAXS (nm-level periodicities). The WAXS rings are from Bragg diffraction from regularly arranged atoms in each of the array of HAP crystals, whereas the SAXS rings originate from scattering due to electron density differences between the periodically arranged HAP crystals and the collagen matrix framework.^[28] The setup for mechanical testing and scattering measurements is similar to previous works.^[30,32] The WAXS patterns were recorded by a GE-41RT flat-panel detector (2048×2048 pixels, $200 \mu\text{m}^2 \text{pixel}^{-1}$), placed 1118 mm from the sample, while the SAXS patterns were recorded by a PI-CCD detector (1152×1242 pixels, $22.5 \mu\text{m} \text{pixel}^{-1}$) placed 4000 mm from the sample. X-ray with a beam size of $50 \times 50 \mu\text{m}^2$ and 70 keV energy was used for the measurements. The X-ray exposure was 1 s for a single WAXS or SAXS measurement, resulting in a dose of 0.6 kGy for a combined WAXS and SAXS measurement (see Appendix for calculation). These X-ray exposure times were as short as possible in order to keep irradiation damage below threshold levels as determined in our previous work.^[30,33]

1.3. Young's Modulus Measurements

Young's moduli of the samples were determined in a separate experiment after the scattering measurements on four samples from the antero-medial, five from the antero-lateral, and five from the postero-lateral quadrants. Strain gages were attached to each of these samples to measure longitudinal strains. The samples were loaded to 60 MPa in 100 s at ambient temperature. This rate of loading is higher than the quasi-static loading carried out during in situ diffraction and mechanical testing, where the samples were held at each load for 246 s to allow time for the diffraction measurements at five different locations on each sample. Also, the samples were not kept hydrated during these macroscopic measurements so as to keep the strain gage adhered to the bone surface during testing. This resulted in the drying of the samples as the experiment proceeded. The total duration of the macroscopic modulus measurements was about 10–15 min which included loading of the samples, and measurement. However, according to the work of Sedlin,^[24] on bending properties of human cortical bone, the elastic modulus did not change significantly for air drying up to 60 min. Thus the duration for which the samples underwent drying is not expected to significantly affect the measured modulus. Also, since the gage section of the each sample was hand-machined, any non-uniformity in the cross-section of the gage region of the sample will be propagated, resulting in the variation of the measured modulus from its actual value (in the case of a perfectly uniform cross-section).

An aluminum (2024-T3 alloy) standard sample, of the same shape and size as the bone samples, was tested first using a strain gage which measured longitudinal strains. The standard sample was loaded up to 75 MPa in load-control, in 100, 200, or 1000 s. The resulting Young's moduli values did not depend on loading rate and averaged 81.9 ± 0.9 GPa, about 12% higher than the literature value of 73.1 GPa.^[38] The bone

Young's modulus reported in Section 3.2 is corrected by this percentage difference.

1.4. Absorption Measurements Using Micro-Computed Tomography

Synchrotron micro-CT was performed on the bone samples at station 2-BM at APS. Due to beam-time limitations, 5 of 25 samples could not be imaged. The bone samples were air-dried overnight after mechanical testing to reduce motion artifacts due to drying. The samples were imaged with 20.7 keV X-rays and reconstructed with $2.9\ \mu\text{m}$ isotropic volume elements (voxels). A total of 1024 $(2\text{K})^2$ slices were recorded and covered 2.9 mm of the sample length (green rectangular box in Figure 1) and one of the positions where the scattering measurements were previously performed (Location 5 in Figure 1).

The reconstructed 2D slices were visualized using ImageJ. Each reconstructed slice is a map of the linear attenuation coefficient. For each specimen, the mean linear attenuation coefficient was calculated for each of six slices spaced 0.29 mm apart. The mean for each sample was the average of the slice average values. The slices near the top and bottom of the imaged volume were not included in this analysis because of low contrast.

Porosity was quantified in the same six slices of each sample. The area fraction of voids was calculated for the entire bone cross-section of each slice using the same segmentation threshold. Each specimen's porosity was the average of its six slices. The microstructure of the sample was determined from the reconstructed image slices. All the samples examined either had a plexiform or a Haversian microstructure corresponding to a microstructure index of zero or one, respectively.

1.5. Thermogravimetric Measurements

Thermogravimetric analysis (TGA) was performed on all 25 samples to determine the volume fractions of the three phases – HAP, collagen, and water – in bone. This was performed using a Mettler-Toledo instrument calibrated with pure In and Al standards. TGA samples, weighing approximately 3–10 mg, were cut from the bone samples after mechanical testing, close to Location 5 sampled by the X-ray beam (Figure 1). They were heated from 25 to 680 °C at a rate of $10\ ^\circ\text{C}\ \text{min}^{-1}$ in air following earlier TGA procedures for bone.^[34,39] As in these studies, the TGA mass loss curves exhibit three distinct regions. The difference in the mass of the sample between two transition temperatures (25, 205, and 545 °C) gives the weight fractions of water, collagen and HAP. These weight fractions are then converted into volume fractions using densities of $1.0\ \text{g}\ \text{cm}^{-3}$ for water, $1.1\ \text{g}\ \text{cm}^{-3}$ for collagen, and $3.2\ \text{g}\ \text{cm}^{-3}$ for HAP.^[1]

1.6. Scattering Analysis

The X-ray scattering data analysis has been described in our previous studies and will be summarized here briefly.^[28,30] The WAXS diffraction patterns are calibrated using a pressed

ceria powder disk. The radial center of the 00.2 peak is determined at each azimuthal angle. The longitudinal HAP strains are determined using the radii at azimuths of $90^\circ \pm 10^\circ$ and $270^\circ \pm 10^\circ$.^[28] The analysis of the SAXS data proceeds in a similar way by determining the radial center of the third order D-period peak at approximately $67/3 = 22.3\ \text{nm}$. The longitudinal strains at a particular stress are calculated by taking an average over $\pm 15^\circ$ about the maximum peak intensity at 90° and 270° azimuths. The WAXS and SAXS strains are reported as a function of stress; the slope of this plot is calculated by taking a linear best-fit and termed as the HAP and fibrillar apparent modulus, respectively.^[30] Data points which deviated grossly from linearity, either at the highest or lowest stresses, were not used for this best-fit slope determination. In all these cases, at least five data points were used for least-squares slope determination.

The azimuthal angle of the maximum intensity of the 00.2 diffraction ring was quantified for all positions on all specimens before loading. The azimuthal full-width at half-maximum intensity (η -FWHM) was also measured for each ring maxima.

1.7. Statistical Analysis

Significant differences in the means of the HAP and fibrillar apparent moduli for different populations were accepted at a significance level of $p < 0.05$ by the one-way ANOVA (Analysis Of Variance) method, using OriginPro 8.6 (Origin Lab, Northampton, MA, USA). In cases where significant differences were measured, pair-wise *t*-tests were used to determine which of the population means differed, also at $p < 0.05$.

In Table 1, when continuously varying data was compared with categorical data, i.e., microstructure index (two categories), the former was separated into the two categories, and significant differences and correlation coefficients were determined using ANOVA.

1.8. Finite Element Modeling

The non-uniform cross-sections at Locations 1–5 in the dog-bone shaped samples result in non-uniform distribution of stress. Finite element analysis was used to determine the distribution of stresses within the samples. The longitudinal stresses were averaged in the direction of travel of the X-ray beam through the sample, i.e., along the 1.5 mm thickness direction, to obtain the average longitudinal stresses at different measurement locations.

The finite element simulation was implemented using ABAQUS 6.10-EF1. The geometry in the model reproduced the dimensions of the dog-bone shaped samples used for the experiments (see Figure 1): 5.0 mm \times 5.0 mm for the gripping region, 2.0 mm width \times 5.0 mm length for the central gage region; the two 7.5-mm long shoulder regions between the gripping and gage regions were connected by smooth curves. The curves were obtained by connecting the width values determined through the optical microscope at the locations at which X-ray scattering measurements were done (3.96 mm

Table 1. Pearson's correlation coefficients for HAP, fibrillar, and Young's moduli, attenuation coefficient (μ), porosity, microstructure index, and HAP volume fraction in the samples. The microstructure index takes a value of zero or unity, respectively, for plexiform or Haversian microstructure.

R	HAP modulus	Fibrillar modulus	Macroscopic modulus	Attenuation coefficient	HAP fraction	Porosity fraction
Fibrillar modulus	0.42					
Macroscopic modulus	0.31	0.17				
Attenuation coefficient	0.14	-0.11	0.55			
HAP fraction	0.20	-0.04	0.66	0.90		
Porosity fraction	-0.30	-0.27	-0.51	-0.55	-0.72	
Microstructure	-0.50	-0.10	-0.67	-0.69	-0.73	0.67

The values indicated in bold are significant at $p < 0.05$, those in italics are significant at $p < 0.3$, and the rest are all $p > 0.3$.

at Location 1, 3.30 mm at Location 2, 2.75 mm at Location 3, 2.37 mm at Location 4, and 2.14 mm at Location 5); the thickness of the sample was set at 1.45 mm, the average thickness of all samples. Since the maximum experimental stress (<60 MPa) was well below the fracture value, only elastic properties were considered (Young's modulus $E = 20 \text{ GPa}^{[40]}$ and Poisson's ratio $\nu = 0.35^{[41]}$). Two types of loads were considered in the simulation: longitudinal tensile load and the gripping stress due to the tensile grips at the gripping region ($5.0 \times 5.0 \text{ mm}^2$). Since the gripping stress used during the measurement was not quantified, the effect of varying it upon the longitudinal stress distribution within the sample was investigated. The model was meshed into C3D8R elements and only the top half of the sample was simulated to increase the efficiency of the calculation, as shown in Figure 1.

2. Results

2.1. Stress Determination

As described in Section 2.2 and illustrated in bottom half of Figure 1, four of five points were measured in the bottom shoulder of the sample and one in the gage region. The longitudinal stresses from finite element simulation are shown for the central plane of the specimen in the top half of the sample in Figure 1. The locations of the diffraction measurements are overlaid on the stress distribution for illustration purposes. Due to the different cross-section areas, the gage region has a higher longitudinal stress while that in the gripping region is lower. Edge effects cause the stress contours to curve. To obtain the longitudinal stresses at Locations 1–5, the stress data were computed in 0.05 mm intervals along the X-ray path and averaged. Since the exact gripping force was not measured during the tensile loading experiments, five different gripping stresses (0, 10, 30, 50, 70 MPa in the $5 \times 5 \text{ mm}^2$ gripping region) were simulated. Figure 2 shows the average longitudinal stress (computed from simulations) versus uniaxial gage section stress, for the cases of minimal and maximal gripping stress (0 and 70 MPa) at two different locations (Locations 1 and 5, closest to and farthest from the gripping region, respectively). The effect of gripping is negligible and the difference of longitudinal stresses between

two extreme cases (0 versus 70 MPa) is less than 3% for all locations on the sample. Therefore, the average longitudinal stresses are calculated with a gripping stress of 30 MPa (an intermediate value).

These average longitudinal stresses are calculated as a function of the load applied on the sample experimentally, i.e., in the range of 0–180 N. These average longitudinal stresses vary linearly with the applied load, as illustrated in Figure 2 (where the x-axis shows the gage stress, defined as load divided by the cross-section of the 5 mm gage area, Figure 1); a linear best-fit for stress versus load is obtained for each measurement location. For the series of gage stresses to which the samples were subjected, the accurate load values were determined for each sample using the equations obtained from the linear best-fits for each location and the measured gage cross-section.

2.2. Intra-sample Variation

A representative plot of phase strain as a function of stress for a single sample is shown in Figure 3a for HAP strain at the

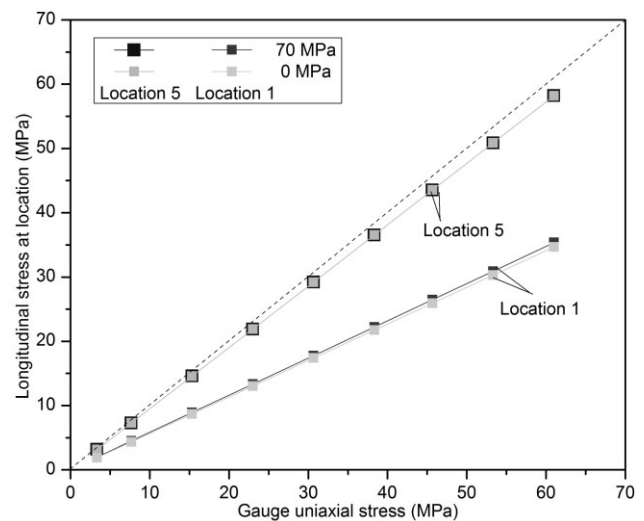


Fig. 2. Plot of average longitudinal stresses versus uniaxial gage stresses, showing effect of gripping compressive stress on the average longitudinal stress at Locations 1 and 5 in the samples.

five locations, and in Figure 3b for fibrillar strain at four locations. The fibrillar strains at Location 4 in this sample were very scattered and hence not shown here. For this sample, $E_{\text{HAP}}^{\text{app}}$ is 19.2 ± 2.9 GPa and $E_{\text{Fib}}^{\text{app}}$ is 3.0 ± 1.4 GPa, as averaged over the five locations (four locations for fibrillar modulus). Figure 3c shows a box plot of the apparent HAP moduli ($E_{\text{HAP}}^{\text{app}}$) measured over all 25 samples and at all five locations in each sample, corresponding to 125 data points. In the case of fibrillar moduli, sample AL8 had very weak scattered intensity from all five locations in the SAXS, and the peak-fits were very poor; this sample was eliminated from $E_{\text{Fib}}^{\text{app}}$ averages. Additionally, 19 other $E_{\text{Fib}}^{\text{app}}$ values were eliminated (6 from Location 1, 3 from Location 2, 2 from Location 3, 6 from Location 4, and 2 from Location 5) because the fitted strain values were very scattered from one stress to another.

Figure 3d thus shows a box plot for a total of 101 $E_{\text{Fib}}^{\text{app}}$ from 24 samples. Statistical analysis (Section 2.7) was performed on $E_{\text{HAP}}^{\text{app}}$ values grouped according to their five positions, in all samples. At Location 5, $E_{\text{HAP}}^{\text{app}}$ is significantly greater than at Locations 1, 2, and 3 ($p < 0.05$); $E_{\text{HAP}}^{\text{app}}$ at Location 4 is significantly greater than at Location 1; $E_{\text{HAP}}^{\text{app}}$ at Location 2 is significantly greater than at Location 1. The fibrillar moduli ($E_{\text{Fib}}^{\text{app}}$) do not differ significantly between the five locations. The average intra-sample standard deviation for apparent elastic modulus across the five locations in each sample is 4.1 GPa for HAP and 1.6 GPa for the fibrils. Because systematically increasing or decreasing trends with position are not found in the HAP or fibrillar apparent moduli, the mean of these five measurement locations hereafter are used when comparing specimens.

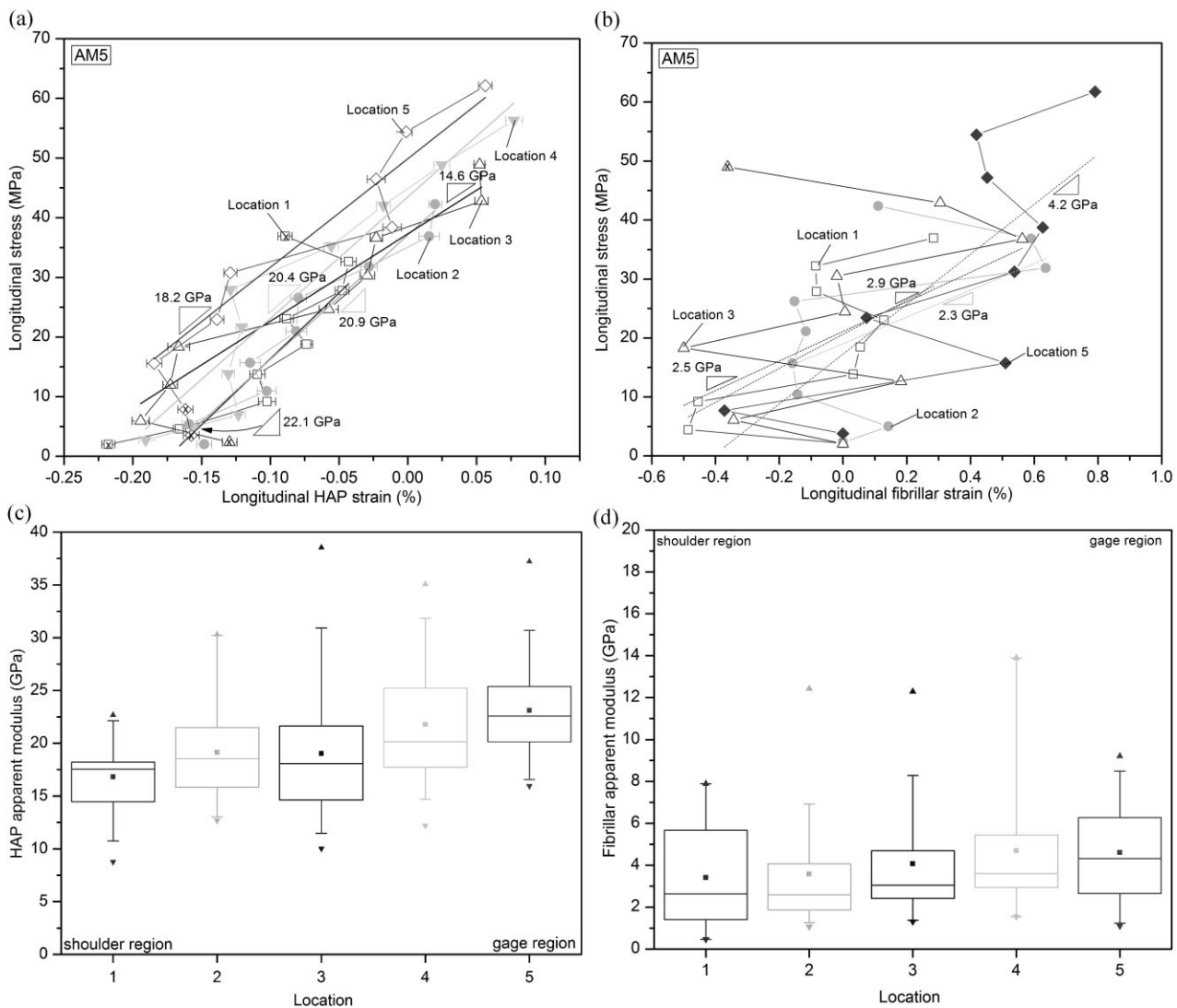


Fig. 3. Plots of longitudinal stress versus (a) HAP strain for all five locations in sample AM5. (b) Fibrillar strain for four locations in sample AM5. Best fit line gives the apparent HAP and fibrillar modulus at each location. Crosses indicate the data points not used for slope determination. (c) Box plot showing the distribution of apparent HAP modulus ($n = 25$ for each box) (d) Box plot for apparent fibrillar modulus ($n = 18, 21, 22, 18,$ and 22 in order of Locations 1–5). The solid line within the box is the median of the distribution, (■) is the mean, (▲▼) are the maximum and minimum values. The whiskers extend out to the 95th and 5th percentiles, and the box represents the 75th, 50th, and 25th percentiles.

2.3. Moduli and Anatomical Position

The apparent HAP moduli were first grouped according to their position in the femur cross-section: anterior (which includes antero-medial and antero-lateral quadrants) or posterior (which has only the postero-lateral quadrant). Figure 4 shows a box plot of the HAP and fibrillar moduli which includes all five locations (three to five locations for fibrils) measured in each sample. No statistically significant difference exists between E_{HAP}^{app} of the anterior (19.7 ± 6.0 GPa, $n=80$) and posterior (20.4 ± 4.4 , $n=45$) sides. The fibrillar apparent moduli, on the other hand, are significantly higher at the anterior side (4.7 ± 2.8 GPa, $n=67$) than the posterior side (2.9 ± 1.8 GPa, $n=33$) as seen in Figure 4.

The moduli were then grouped according to their quadrants, i.e., antero-medial, antero-lateral, and postero-lateral. As seen in Figure 5, the HAP apparent moduli in the antero-lateral quadrant (17.4 ± 4.1 GPa, $n=50$) are significantly lower than those in the antero-medial (23.6 ± 6.6 GPa, $n=30$) ($p < 0.001$) and the postero-lateral quadrant (20.4 ± 4.4 GPa, $n=45$) ($p = 0.001$). Also, the HAP apparent moduli in the antero-medial quadrant are significantly greater than the posterior-lateral quadrant ($p = 0.013$). A quadrant-wise comparison of the fibrillar apparent moduli also showed (Figure 5) that the values in the antero-medial quadrant (5.8 ± 3.0 GPa, $n=28$) were significantly greater than the antero-lateral (3.9 ± 2.3 GPa, $n=39$) ($p = 0.006$) and the posterior-lateral (2.9 ± 1.9 GPa, $n=33$) quadrants ($p < 0.001$). The fibrillar apparent moduli in the antero-lateral quadrant are significantly greater than in the posterior-lateral quadrant ($p = 0.036$). The average macroscopic Young's modulus (E_{macro}) in the antero-medial quadrant (31.1 ± 6.0 GPa, $n=4$) is also greater than the antero-lateral quadrant (17.5 ± 5.2 GPa, $n=5$) ($p = 0.009$), and the antero-lateral quadrant is lower than the posterior-lateral quadrant (25.9 ± 5.8 GPa, $n=5$) ($p = 0.044$). A similar grouping was done with the corresponding η -FWHM of the samples to

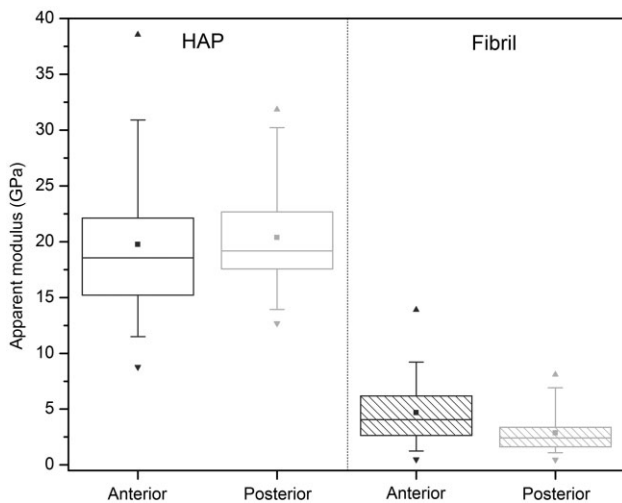


Fig. 4. Box plot of the HAP ($n=80$ and 45 left to right) and fibrillar ($n=68$ and 33 left to right) apparent modulus for anterior and posterior samples. Signification of boxes, symbols, and lines are as in Figure 3b and c.

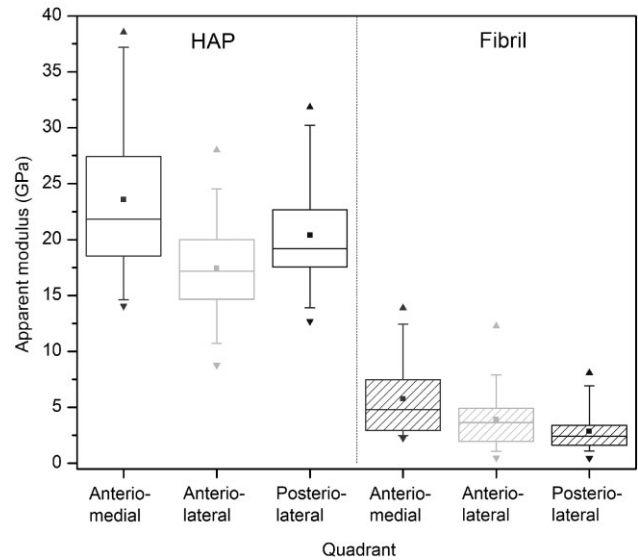


Fig. 5. Box plot of the quadrant-wise comparison of the HAP ($n=30, 50,$ and 45 left to right) and fibrillar ($n=28, 40,$ and 33 left to right) apparent moduli for all the samples. Signification of boxes, symbols and lines are as in Figure 3b and c.

determine any significant differences between the quadrants. The antero-medial quadrant had significantly lower η -FWHM values ($53^\circ \pm 4^\circ$) than the antero-lateral ($57^\circ \pm 6^\circ$) ($p = 0.003$) and the postero-lateral ($61^\circ \pm 8^\circ$) quadrants ($p < 0.001$). One single sample (AL8) had a η -FWHM value of $112^\circ \pm 23^\circ$. The maximum intensity azimuthal angle is found to vary from 70° to 120° in most samples and was 140° in one single case (AL8), indicating that the (00.l) peak was not perfectly aligned with the loading/longitudinal direction.

Figure 6 shows the HAP and fibrillar apparent moduli, E_{HAP}^{app} and E_{Fib}^{app} , and the E_{macro} for the different samples measured. By averaging the slopes from all of the five locations for HAP, and three to five locations for fibrils, from all of the 25 samples for HAP (125 slopes), and 24 samples for fibrils (101 slopes), the overall HAP and fibrillar moduli were calculated to be 20.0 ± 5.4 and 4.1 ± 2.6 GPa, respectively (dotted lines in Figure 6). The average value of the E_{macro} obtained over 14 samples is 21.5 ± 6.8 GPa (dotted line in Figure 6). The large spread in the apparent moduli values reflects positional variations within individual samples. The inter-sample standard deviations calculated between the average apparent elastic moduli measured for each sample are 3.7 GPa for HAP, and 2.1 GPa for the fibrils. These inter-sample variations are similar to the observed intra-sample variations of 4.1 and 1.6 GPa for HAP and fibrils, respectively (Section 3.2). It is apparent that the mean macroscopic Young's modulus is lower in the antero-lateral quadrant compared to the antero-medial and posterior-lateral quadrants. This trend is also exhibited by both the HAP and fibrillar apparent moduli.

2.4. Microstructure

The reconstructed slices in Figure 6 show representative microstructures from two samples, AL7 and PL4, which have a

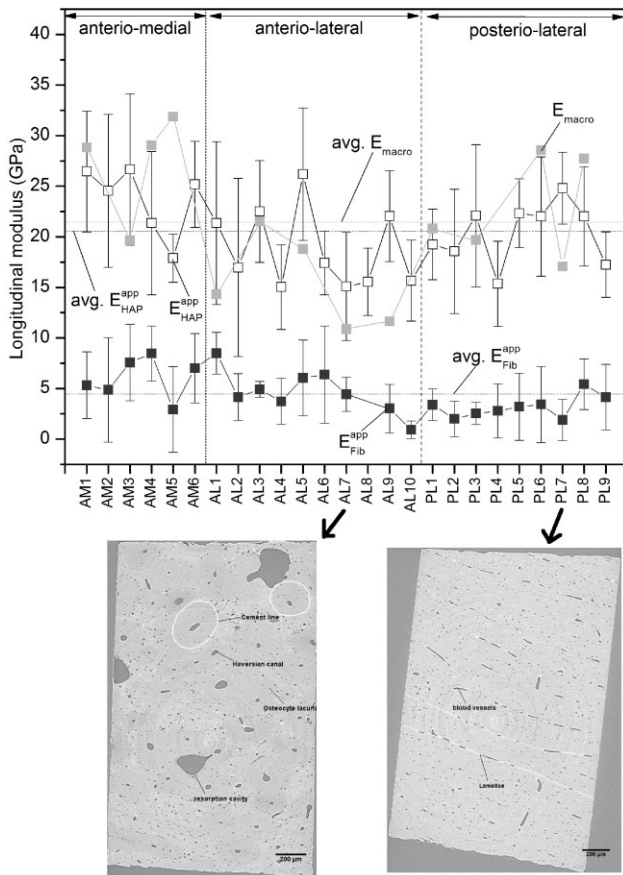


Fig. 6. Plot of HAP ($n = 25$) and fibrillar ($n = 24$) apparent moduli and macroscopic Young's modulus ($n = 14$) of all the samples. The HAP and fibrillar moduli of each sample are averaged over the five and three to five different locations measured, respectively. The horizontal dashed lines give the average of each type of modulus. The microstructures below show an example of the Haversian (left) and plexiform (right) type, obtained from micro-CT. Two osteons in the Haversian and a lamellar unit in the plexiform structure are highlighted in the respective microstructures.

Haversian and plexiform microstructure, respectively. This typical Haversian microstructure shows multiple lightly mineralized osteons scattered across the cross-section. Two osteons are outlined in the slice from sample AL7. The plexiform microstructure on the other hand has uniformly arranged lamellar units enclosing blood vessels; one lamellar unit is outlined in the slice of sample PL4. The average value of the linear attenuation coefficient from all the samples is $7.40 \pm 0.15 \text{ cm}^{-1}$. By way of comparison, the mean and standard deviation of the linear attenuation coefficient in sample AL7 is $6.93 \pm 0.06 \text{ cm}^{-1}$ and that in PL4 is $7.48 \pm 0.08 \text{ cm}^{-1}$. At 20.7 keV, the tabulated value of the linear attenuation coefficient for cortical bone (ICRU-44) from the NIST database is 7.23 cm^{-1} assuming a density of 1.92 g cm^{-3} .^[42] Thus, the values obtained for cortical bone in the current experiment are within the same range as the standard values. The average porosity in the bone samples is $5.0 \pm 2.0\%$ and is at the lower range of porosity values (5–10%), commonly found in cortical bone.^[43] The average porosity found in the samples with Haversian microstructure is $8.0 \pm 3.5\%$ and that in the samples with plexiform microstructure is $4.4 \pm 1.1\%$. The $12.0 \pm 1.9\%$ poros-

ity in sample AL8 (Haversian microstructure) was much higher than the average. In sample AL7 with Haversian microstructure in Figure 6, of a total porosity of 6.7%, the porosity due to osteocyte lacunae, Haversian canals, and resorption cavities is 2.3 ± 0.3 , 2.1 ± 0.5 , and $2.2 \pm 0.5\%$, respectively. In sample PL4 with a plexiform microstructure in Figure 6, of a total porosity of 3.4%, the porosity due to osteocyte lacunae and blood vessels is $1.7 \pm 0.1\%$ each.

2.5. Correlation between Moduli and Structure

The correlation coefficients between the HAP, fibrillar and Young's moduli with porosity, HAP volume fraction and linear attenuation coefficients are listed in Table 1. The most significant correlations are found for the HAP modulus which correlates positively with the fibril modulus ($R = 0.42$), and negatively with the microstructure index ($R = -0.50$). Thus, the HAP apparent moduli were lower for sample with the Haversian-type ($15.3 \pm 2.3 \text{ GPa}$, $n = 3$) compared to the plexiform-type ($20.9 \pm 3.8 \text{ GPa}$, $n = 17$) microstructure. The fibrillar apparent moduli on the other hand were in the same range for both types of microstructures, i.e., $3.4 \pm 0.2 \text{ GPa}$ ($n = 2$) and $4.0 \pm 2.1 \text{ GPa}$ ($n = 17$) for Haversian and plexiform-type, respectively. Young's modulus also increases significantly with increase in HAP volume fraction ($R = 0.66$) and decrease in microstructure index ($R = -0.67$). Three out of the 20 samples imaged (labeled AL2, AL7, and AL8) exhibited Haversian-type microstructure; the other 17 samples had a plexiform-type microstructure. Macroscopic Young's modulus was obtained on a total of 14 samples, but there were only nine samples which had both Young's modulus and microstructure information. Of these nine samples, only sample AL7 exhibited a Haversian-type microstructure, and it had a lower Young's modulus ($10.9 \pm 0.1 \text{ GPa}$) than the other eight samples with a plexiform-type microstructure ($24.5 \pm 5.9 \text{ GPa}$). Finally, the linear attenuation coefficient significantly correlates with the HAP volume fraction ($R = 0.90$), porosity ($R = -0.55$) and microstructure index ($R = -0.69$). Other variables exhibit slightly weaker correlations with each other, as seen from Table 1.

3. Discussion

3.1. Deformation Mechanism

The average HAP and fibrillar apparent moduli in the present work are 20.0 ± 5.4 ($n = 125$) and 4.1 ± 2.6 ($n = 101$) GPa, respectively. These values are significantly lower than values from compression, tested from the same femur,^[34] of $E_{\text{HAP}}^{\text{app}}$ ($27.5 \pm 6.6 \text{ GPa}$, $n = 120$) or $E_{\text{Fib}}^{\text{app}}$ ($18.5 \pm 8.9 \text{ GPa}$, $n = 100$).^[30] The lower values of $E_{\text{HAP}}^{\text{app}}$ and $E_{\text{Fib}}^{\text{app}}$ under tensile loading indicate that the fibrils and the HAP carry higher strains (which are elastic for HAP and elasto-plastic for fibrils^[32]), for a given stress, compared to compressive loading. The higher HAP strains during tensile deformation indicate a higher level of load transfer from the protein matrix, which is usually associated with a lower strength matrix. This is confirmed by the higher fibril strains, which also indicate a weaker matrix in tension.

COMMUNICATION

The average macroscopic Young's modulus in the present study is 21.5 ± 6.8 GPa ($n=14$) which is within the broad range of values, 18–32 GPa, found in literature for cortical bones of species such as bovine, equine, human, deer, etc., loaded in tension.^[12,44] The tensile average Young's modulus found in the present study is not significantly different ($p < 0.05$) from the compressive value of 20.5 ± 1.5 GPa ($n=23$) found in our previous study on samples taken from the same animal.^[34] As discussed in Section 1, there is no general agreement in the literature about the association between the macroscopic tensile and compressive modulus. Also, the compressive Young's modulus is measured using the ultrasonic speed-of-sound technique. Grimal *et al.*^[45] have reported that the ultrasonic modulus of cortical bone is about 21% higher than the modulus determined from mechanical testing (three-point bend tests) due to stress-relaxation effects. Thus, the difference between the compressive (20.5 ± 1.5 GPa) and tensile Young's modulus (21.5 ± 6.8 GPa) in the present case could also result from the experimental variations between the two techniques.

The flat dog-bone-shaped specimens in the present experiment were loaded to the maximum 180 N (equivalent approximately to a longitudinal stress of 60 MPa at Location 5), thus resulting in a maximum macroscopic strain of about $0.060/21.5 = 0.0028$ (0.28%). In recent work by Hoo *et al.* on bovine femoral bone,^[27] it was shown that a sudden decrease in the longitudinal HAP and fibrillar strains occurs beyond a macroscopic tensile strain of 0.2%, and this was hypothesized to occur due to localized plastic deformation; the macroscopic stress-strain curve did not show any deviation from linearity at this point. It was theorized that stress is redistributed from longitudinally oriented and load-bearing mineralized collagen fibrils to the laterally oriented nanoscale structures, without affecting the total strain carried by the material.^[27] Similarly, we hypothesize here that localized plastic deformation takes place at the molecular collagen level which results in large strains measured within the fibrils. The increased plastic deformation within the collagen matrix results in a decrease in the $E_{\text{Fib}}^{\text{app}}$. The HAP/collagen interface is expected to be minimally damaged due to irradiation because of the low exposure times used to acquire X-ray scattering data.^[30] There could be loss of some van der Waals or hydrogen bonds at the interface due to mechanical loading which would weaken the interface,^[30] thus decreasing load transfer from collagen to HAP to some extent. However, the observed increase in load transfer, and hence strain, to the reinforcement (HAP) results in lower values of apparent moduli compared to compression experiments.

The greater strain which is carried under tensile loading by both phases also suggests that the collagen phase (being more compliant than HAP) yields at lower stresses than under compressive loading. The ratio of fibril to mineral strain in the present work is calculated as 4:1, and is about 1.6–3.5 times higher than the value of 5:2, for tensile testing on fibrolamellar packets of bovine femoral bone, found by Gupta *et al.*,^[31] and 8:7 for tensile testing on fibrolamellar bovine femoral bones,

found by Hoo *et al.*^[27] The difference in the ratios can be attributed to the different testing conditions [dried^[27] versus hydrated (present case)] and the influence of the structures present at larger length scales, e.g., osteons, due to large (millimeter-sized) samples being studied in the present case compared to thin lamellar (50–100 μm thick) sections of bone studied in ref.^[31] Our previous work on compressive loading of bovine bone samples, which were taken from the same animal as the samples in the present work, results in a fibril to mineral strain ratio of 8:5.^[34] This further confirms that the fibrils deform to a much larger extent under tensile loading. Furthermore, the fact that moduli in the present work are being compared between samples taken from the same animal, makes a strong case for the above finding, rather than two studies on two different animals.

The mechanical properties of collagen obtained from a variety of species, demineralized bone, and in vitro self-assembled fibrils have been extensively characterized. The extraction of individual collagen fibrils in their native state poses a major challenge to the determination of its properties. The most commonly found values for the Young's modulus of collagen range from 2 to 11 GPa when tested in ambient conditions,^[46] and 0.2–0.8 GPa under hydrated conditions.^[47,48] Whereas a lot of research has been performed on collagen under tensile loading, almost no information exists on its properties under compression. It is difficult to test collagen under compressive loading due to its lack of rigidity in the longitudinal direction.^[47] However, it is reasonable to assume that the behavior of collagen is different under tensile and compressive loading because of its highly fibrous structure which influences the overall load transfer behavior. According to the studies of Dempster and Liddicoat on human femurs,^[16] plastic deformation of bone begins at about 36 MPa in tension and 70 MPa in compression. Greater strains and thus greater plastic deformation are then expected for collagen fibrils loaded in tension. Moreover, since cortical bone is predominantly loaded in compression or bending under natural physiological circumstances, it has evolved to resist compressive loads more effectively than tensile loads.^[1,2]

3.2. Spatial Variations between Femur Quadrants

A comparison of Young's moduli of samples taken from three quadrants of the femur (Figure 6) shows that the antero-lateral region is significantly less stiff, in macroscopic tension, compared with the antero-medial and posterior-lateral regions. This trend is also exhibited by the statistically significant lower $E_{\text{HAP}}^{\text{app}}$ in the antero-lateral quadrant. This suggests that the Young's modulus and $E_{\text{HAP}}^{\text{app}}$ depends on similar factors as discussed in the following. The larger variation in $E_{\text{Fib}}^{\text{app}}$ (Figure 6b), on the other hand, obscure any trend. The lower azimuthal spread (FWHM) in the HAP 00.2 diffraction ring, and hence the orientation distribution of HAP *c*-axes with respect to the longitudinal/loading direction, in the antero-medial region, compared to the antero- and posterior-lateral regions, is consistent with the lower $E_{\text{HAP}}^{\text{app}}$ in the latter two regions. The anisotropic elastic constants of

HAP have been reported as $C_{11} = 137$ GPa and $C_{33} = 172$ GPa in Katz and Ukrainci,^[49] with the c -axis aligned along the 33 direction, which makes it the most load bearing direction. Thus when there are fewer HAP platelets with c -axes aligned with the longitudinal (or loading) direction in the sampled volume, as in the antero- and posterior-lateral quadrants, the average strain on those HAP platelets increases, thus decreasing the measured $E_{\text{HAP}}^{\text{app}}$.

The HAP, fibrillar, and Young's moduli exhibit significant correlations with the microstructure, porosity, HAP volume fraction and the mean attenuation coefficient (Table 1). The Young's modulus of the sample increases with the HAP content ($R = 0.66$), which is a good predictor of bone stiffness.^[19,20] This is similar to the behavior of a short-fiber reinforced composite, where an increase in the stiffer reinforcement content (HAP in this case) results in an increase in the overall stiffness of the sample. As expected, the linear attenuation coefficient, which reflects the mineral content of specimen, also correlates with HAP volume fraction ($R = 0.90$). Thus, linear attenuation coefficient also increases the Young's modulus ($R = 0.55$). The HAP apparent modulus concomitantly increases with the Young's modulus ($R = 0.31$), but correlates much less significantly with the HAP fraction ($R = 0.20$). For the latter correlation, as the fraction of stiff HAP platelets increases, the average stress on each HAP platelet decreases, resulting in an increase in the HAP apparent modulus ($= \sigma_{\text{applied}} / \epsilon_{\text{phase}}$). However, as compared to the Young's modulus, $E_{\text{HAP}}^{\text{app}}$ increases less significantly with HAP fraction ($R = 0.2$ versus 0.66). This may be because the samples used to determine the HAP fraction are obtained approximately from the region sampled by the X-ray beam, and that region might not be completely representative of the local volume fractions everywhere in the bulk sample.^[34] Also, an increase in the HAP apparent modulus is accompanied by an increase in the fibrillar apparent modulus ($R = 0.42$). The HAP modulus reflects the ability of the HAP phase to bear load; the fibrillar modulus applies to an HAP/collagen nano-composite, and reflects the cooperative deformation between HAP and collagen. Greater load carrying capacity of the HAP phase thus increases the load carrying capacity of the whole fibril due to factors discussed above. Thus, the correlation between fibrillar modulus and HAP modulus is expected.

The distribution of microstructures in the transverse cross-section of the femur used in the present experiment is such that specimens of plexiform structure are found in most of the antero-medial, antero-lateral, and posterior-lateral regions. Specimens of Haversian structure are found in the anterior and lateral ends of the femur cross-section. These results are consistent with that of ref.^[50], which reported a similar relation between the spatial location and bone microstructure. The correlation of microstructure with sample porosity ($R = 0.67$) indicates that Haversian bone has greater porosity than plexiform bone (8.0 versus 4.4% volume fractions, respectively), which makes Haversian bone less stiff both macroscopically ($R = -0.67$) and at the nanoscale

level ($E_{\text{HAP}}^{\text{app}}$, $R = -0.50$). Haversian bone is also less mineralized compared to plexiform bone, as indicated by the lower attenuation coefficient ($R = -0.69$) and lower HAP fraction ($R = -0.73$). The higher porosity and lower mineral content of Haversian bone thus results in lower moduli (samples AL2, AL7, and AL8) compared to plexiform bone.^[51] Among all the samples tested, the Young's modulus is determined only for a single Haversian bone sample. This limitation can however be circumvented by considering the fact that the same trend is exhibited by both Young's modulus and $E_{\text{HAP}}^{\text{app}}$ with respect to the microstructure, thus confirming that plexiform bone is stiffer than Haversian bone.

The distribution of moduli in the various quadrants of the femur (Figure 6) is most probably a result of the physiological needs of the animal.^[52] As bone forms and remodels according to the stresses experienced locally,^[1,53] a region which experiences higher stresses becomes reinforced to a greater extent through the addition of HAP, and attains a higher stiffness. Similarly a region which experiences more impact loads might show better shock absorption through introduction of pores. In our previous work,^[34] compressive stiffness was higher for the antero-medial region than for the antero-lateral region. This was attributed to the presence of higher compressive physiological loads experienced by the antero-medial region, resulting in greater HAP volume fractions and thus higher modulus. The higher tensile stiffness of the antero-medial region compared with the antero-lateral region found in the present work confirms this finding. For bovine bones which are predominantly loaded in compression, higher tensile stiffness may be beneficial during a bending action due to the physiological loads with the stress magnitude varying along the length of the femur, depending on the position of the neutral bending axis in the transverse cross-section of the femur,^[54] and the curvature of the femur.^[6] This suggests that the antero-medial region has evolved to withstand higher stresses, both tensile and compressive, in physiological situations.

4. Conclusions

Synchrotron X-ray diffraction was employed to study, for the first time, the level and variability of the nanoscale strain and stress partitioning behavior in bovine bones under tensile loading. The apparent moduli measured at the phase (HAP and fibrillar) level in situ by X-ray scattering, as well as the Young's modulus measured by tensile tests over large volumes, varied significantly between different quadrants of the femur cross-section, with the antero-medial region being the stiffest. These differences correlated with the HAP volume fraction, sample texture, porosity, and microstructure. Comparisons of elastic behavior at the nanoscale level were made, for the first time, between tensile and compressive loading of samples obtained from the same animal. The tensile apparent HAP and fibrillar moduli were significantly lower than in compression, which may be due to the asymmetry of the elasto-plastic properties of collagen in tension and

compression, which affects its load transfer capabilities to the HAP platelets reinforcing it. Collagen is hypothesized to deform plastically by intermolecular sliding to a greater extent under tensile loading, resulting in greater transfer of strains to the HAP and lower HAP apparent moduli of both HAP and fibrils. The variability in the apparent moduli within and between samples measured here underscores the need for sampling over a large population of samples and multiple locations to discern statistically significant trends.

Appendix: Radiation Dose Calculation

These calculations are done following equations described in ref.^[37]. The radiation dose, D , in Grays (Gy) is:

$$D = \frac{E_b \phi t A_{E_n}}{M} \quad (\text{A1})$$

where E_b is the beam energy (1.12×10^{-14} J at an energy of 70 keV), ϕ the photon flux (6.68×10^9 ph s⁻¹), t the exposure time (1 s), and M is the irradiated sample mass (7.2×10^{-9} kg, calculated as the product of the beam area $A = 0.0050^2$ cm² = 2.5×10^{-5} cm², sample thickness $l = 0.15$ cm, and sample density $\rho = 1.96$ g cm⁻³). The sample energy absorption, A_{E_n} , is given as:

$$A_{E_n} = 1 - \exp(-\alpha_{E_n} l \rho) \quad (\text{A2})$$

where α_{E_n} is the mass energy absorption coefficient for cortical bone (0.10 cm² g⁻¹ for cortical bone at 70 keV^[42]). The value of $A_{E_n} = 0.03$ from the above calculation.

Introducing the above parameters into Eq. (A1–A2) gives a radiation dose per individual (WAXS or SAXS) scattering measurement $D = 290$ Gy, and a total dose per combined (WAXS and SAXS) measurement $D = 580$ Gy.

The radiation dose per scattering measurement is therefore 0.29 kGy. The total dose per WAXS and SAXS (2 s) measurement is 0.58 kGy.

Received: June 8, 2012

Final Version: September 12, 2012

Published online: October 23, 2012

- [1] R. B. Martin, D. B. Burr, N. A. Sharkey, *Skeletal Tissue Mechanics*, Springer 1998.
- [2] J. D. Currey, *Bones: Structure and Mechanics*, Princeton University Press, Princeton, NJ 2006.
- [3] S. M. Swartz, J. E. A. Bertram, A. A. Biewener, *Nature* 1989, 342, 270.
- [4] D. Paley, *J. Pediatr. Orthop.* 1988, 8, 73.
- [5] a) L. E. Lanyon, R. N. Smith, *Acta Orthop. Scand.* 1970, 41, 238. b) L. E. Lanyon, W. G. J. Hampson, A. E. Goodship, J. S. Shah, *Acta Orthop. Scand.* 1975, 46, 256. c) C. T. Rubin, L. E. Lanyon, *J. Exp. Biol.* 1982, 101, 187. d) C. T. Rubin, L. E. Lanyon, *J. Theor. Biol.* 1984, 107, 321.
- [6] J. E. A. Bertram, A. A. Biewener, *J. Theor. Biol.* 1988, 131, 75.
- [7] a) L. Lanyon, D. Baggott, *J. Bone Joint Surg. Br.* 1976, 58-B, 436. b) J. G. Skedros, R. D. Bloebaum, M. W. Mason, D. M. Bramble, *Anat. Rec.* 1994, 239, 396.
- [8] M. Bessho, I. Ohnishi, J. Matsuyama, T. Matsumoto, K. Imai, K. Nakamura, *J. Biomech.* 2007, 40, 1745.
- [9] a) D. T. Reilly, A. H. Burstein, *J. Bone Joint Surg.* 1974, 56, 1001. b) J. D. Currey, *J. Exp. Biol.* 1999, 202, 2495.
- [10] V. Ebacher, C. Tang, H. McKay, T. R. Oxland, P. Guy, R. Wang, *Bone* 2007, 40, 1265.
- [11] D. T. Reilly, A. H. Burstein, *J. Biomech.* 1975, 8, 393.
- [12] G. C. Reilly, J. D. Currey, *J. Exp. Biol.* 1999, 202, 543.
- [13] A. Matzenmiller, J. Lubliner, R. L. Taylor, *Mech. Mater.* 1995, 20, 125.
- [14] M. M. Barak, J. D. Currey, S. Weiner, R. Shahar, *J. Mech. Behav. Biomed. Mater.* 2009, 2, 51.
- [15] C. M. Riggs, L. C. Vaughan, G. P. Evans, L. E. Lanyon, A. Boyde, *Anat. Embryol.* 1993, 187, 239.
- [16] W. T. Dempster, R. T. Liddicoat, *Am. J. Anat.* 1952, 91, 331.
- [17] a) R. W. McCalden, J. A. McGeough, M. B. Barker, C. M. Courtbrown, *J. Bone Joint Surg.-Am. Vol.* 1993, 75A, 1193. b) X. Wang, X. Shen, X. Li, C. Mauli Agrawal, *Bone* 2002, 31, 1.
- [18] a) T. M. Wright, W. C. Hayes, *Med. Biol. Eng. Comput.* 1976, 14, 671. b) H. D. Wagner, S. Weiner, *J. Biomech.* 1992, 25, 1311.
- [19] J. D. Currey, *J. Biomech.* 1988, 21, 131.
- [20] J. D. Currey, *Philos. Trans. R. Soc. Lond. Ser. B, Biol. Sci.* 1984, 304.
- [21] X. N. Dong, X. E. Guo, *J. Biomech.* 2004, 37, 1281.
- [22] J. G. Ramasamy, O. Akkus, *J. Biomech.* 2007, 40, 910.
- [23] a) A. K. Bembey, A. J. Bushby, A. Boyde, V. L. Ferguson, M. L. Oyen, *J. Mater. Res.* 2006, 21, 1962. b) A. K. Bembey, M. L. Oyen, A. J. Bushby, A. Boyde, *Philos. Mag.* 2006, 86, 5691. c) F. S. Utku, E. Klein, H. Saybasili, C. A. Yucesoy, S. Weiner, *J. Struct. Biol.* 2008, 162, 361.
- [24] F. G. Evans, *Mechanical Properties of Bone*, Thomas 1973.
- [25] W. Bonfield, C. H. Li, *J. Biomech.* 1968, 1, 323.
- [26] a) M. L. Young, J. D. Almer, M. R. Daymond, D. R. Haeffner, D. C. Dunand, *Acta Mater.* 2007, 55, 1999. b) M. L. Young, J. DeFouw, J. D. Almer, D. C. Dunand, *Acta Mater.* 2007, 55, 3467. c) M. L. Young, R. Rao, J. D. Almer, D. R. Haeffner, J. A. Lewis, D. C. Dunand, *Acta Mater.* 2009, 57, 2362.
- [27] R. P. Hoo, P. Fratzl, J. E. Daniels, J. W. C. Dunlop, V. Honkimäki, M. Hoffman, *Acta Biomater.* 2011, 7, 2943.
- [28] J. D. Almer, S. R. Stock, *J. Struct. Biol.* 2005, 152, 14.
- [29] a) R. Akhtar, M. R. Daymond, J. D. Almer, P. M. Mummery, *J. Mater. Res.* 2007, 23, 543. b) J. D. Almer, S. R. Stock, *J. Struct. Biol.* 2007, 157, 365. c) X. N. Dong, J. D. Almer, X. Wang, *J. Biomech.* 2011, 44, 676. d) H. S. Gupta, W. Wagermaier, A. Zickler, J. Hartmann, S. S. Funari, P. Roschger, H. D. Wagner, P. Fratzl, *Int. J. Fract.* 2006, 139, 425. e) S. R. Stock, F. Yuan, L. C. Brinson, J. D. Almer, *J. Biomech.* 2011, 44, 291. f) R. Akhtar, M. R. Daymond, J. D. Almer, P. M. Mummery, *Acta Biomater.* 2011, 7, 716.

- [30] A. Singhal, A. Deymier-Black, J. D. Almer, D. C. Dunand, *J. Mech. Behav. Biomed. Mater.* **2011**, *4*, 1774.
- [31] H. S. Gupta, J. Seto, W. Wagermaier, P. Zaslansky, P. Boesecke, P. Fratzl, *PNAS* **2006**, *103*, 17741.
- [32] A. C. Deymier-Black, F. Yuan, A. Singhal, J. D. Almer, L. C. Brinson, D. C. Dunand, *Acta Biomater.* **2011**, *8*, 253.
- [33] H. D. Barth, E. A. Zimmermann, E. Schaible, S. Y. Tang, T. Alliston, R. O. Ritchie, *Biomaterials* **2011**, *32*, 8892.
- [34] A. Singhal, J. D. Almer, D. C. Dunand, *Acta Biomater.* **2012**, *8*, 2747.
- [35] R. Akhtar, M. R. Daymond, J. D. Almer, P. M. Mummery, *Acta Biomater.* **2008**, *4*, 1677.
- [36] a) A. C. Deymier-Black, J. D. Almer, S. R. Stock, D. R. Haeffner, D. C. Dunand, *Acta Biomater.* **2010**, *6*, 2172. b) J. D. Almer, S. R. Stock, *J. Biomech.* **2010**, *43*, 2294. c) A. C. Deymier-Black, J. D. Almer, D. R. Haeffner, D. C. Dunand, *Mater. Sci. Eng., C* **2011**, *31*, 1423.
- [37] A. C. Deymier-Black, S. R. Stock, J. D. Almer, D. C. Dunand, *J. Mech. Behav. Biomed. Mater.* **2012**, *5*, 71.
- [38] M. Bauccio, Ed, *ASM Metals Reference Book*, ASM International, Materials Park, OH **1993**.
- [39] L. F. Lozano, M. A. Pena-Rico, A. Heredia, J. Octolán-Flores, A. Gomez-Cortes, R. Velazquez, I. A. Belio, L. Bucio, *J. Mater. Sci.* **2003**, *38*, 4777.
- [40] J. Y. Rho, R. B. Ashman, C. H. Turner, *J. Biomech.* **1993**, *26*, 111.
- [41] R. B. Ashman, S. C. Cowin, W. C. Van Buskirk, J. C. Rice, *J. Biomech.* **1984**, *17*, 349.
- [42] J. H. Hubbell, S. M. Seltzer, Vol. 2011, National Institute of Standards and Technology, Gaithersburg, MD, <http://physics.nist.gov/xaamdi> **2004**.
- [43] L. J. Gibson, M. F. Ashby, *Cellular Solids – Structure and Properties*, Cambridge University Press **1997**.
- [44] a) J. D. Currey, *J. Exp. Biol.* **1999**, *202*, 3285. b) M. B. Schaffler, E. L. Radin, D. B. Burr, *Bone* **1990**, *11*, 321.
- [45] Q. Grimal, S. Hauptert, D. Mitton, L. Vastel, P. Laugier, *Med. Eng. Phys.* **2009**, *31*, 1140.
- [46] a) J. A. J. van der Rijt, K. O. van der Werf, M. L. Bennink, P. J. Dijkstra, J. Feijen, *Macromol. Biosci.* **2006**, *6*, 697. b) M. P. E. Wenger, L. Bozec, M. A. Horton, P. Mesquida, *Biophys. J.* **2007**, *93*, 1255.
- [47] A. J. Heim, W. G. Matthews, T. J. Koob, *Appl. Phys. Lett.* **2006**, *89*.
- [48] a) S. J. Eppell, B. N. Smith, H. Kahn, R. Ballarini, *J. R. Soc. Interface* **2006**, *3*, 117. b) Z. L. Shen, M. R. Dodge, H. Kahn, R. Ballarini, S. J. Eppell, *Biophys. J.* **2008**, *95*, 3956. c) S. Strasser, A. Zink, M. Janko, W. M. Heckl, S. Thalhammer, *Biochem. Biophys. Res. Commun.* **2007**, *354*, 27.
- [49] J. L. Katz, K. Ukrainci, *J. Biomech.* **1971**, *4*, 221.
- [50] a) Y. Yamato, M. Matsukawa, T. Otani, K. Yamazaki, A. Nagano, *Ultrasonics* **2006**, *44*, e233. b) M. Sasso, G. Haïat, Y. Yamato, S. Naili, M. Matsukawa, *J. Biomech.* **2008**, *41*, 347.
- [51] J. L. Katz, H. S. Yoon, *IEEE Trans. Biomed. Eng.* **1984**, *BME-31*, 878.
- [52] A. A. Espinoza Orías, J. M. Deuerling, M. D. Landrigan, J. E. Renaud, R. K. Roeder, *J. Mech. Behav. Biomed. Mater.* **2009**, *2*, 255.
- [53] S. C. Cowin, *Bone Mechanics*, CTC Press, Boca Raton, FL **1989**.
- [54] G. N. Duda, E. Schneider, E. Y. S. Chao, *J. Biomech.* **1997**, *30*, 933.